Performance Analysis of an Improved Gravity Anchor Bolt Expanded Foundation

applied sciences

MDPI

Article

Performance Analysis of an Improved Gravity Anchor Bolt Expanded Foundation

Zhenli Zhang [1], Qingyang Liu [1,*], Hongmin Chu [1], Giuseppe Lacidogna [2], Jie Xu [3], Haiyang Cheng [3], Zhitao Liu [3] and Weitao Jiang [3]

[1] Shandong Electric Power Engineering Consulting Institute Corp., Ltd., Jinan 250013, China; zhangzhenli@sdepci.com (Z.Z.); chuhongmin@sdepci.com (H.C.)
[2] Department of Structural, Geotechnical and Building Engineering, Politecnico di Torino, 10129 Torino, Italy; giuseppe.lacidogna@polito.it
[3] School of Civil Engineering, Tianjin University, Tianjin 300072, China; jxu@tju.edu.cn (J.X.); nychy2000@tju.edu.cn (H.C.); jwt@tju.edu.cn (W.J.)
* Correspondence: liuqingyang@sdepci.com; Tel.: +86-139-5415-6090

Abstract: With the continuous utilization of renewable energy, the number of onshore wind turbines is increasing. Small design improvements can save costs and facilitate the maintenance and repair of the wind turbine foundation. In this paper, an existing gravity expansion foundation with an anchor cage is improved. Our improvements further expand the space inside the foundation and reduce the length of the anchor bolt, which could reduce the costs and facilitate construction. To study the performance of the new foundation, a three-dimensional finite element model of the foundation–soil–anchor bolt was established via a finite element simulation. The damage evolution of the foundation was simulated with the concrete damage plasticity model (CDP). The separation ratio, foundation settlement, inclination ratio, reinforcement stress, foundation stress, and foundation damage of the new foundation under ultimate load conditions were analyzed. The influence of parameters h1 and b3 on the performance of the foundation was further studied. The finite element analysis results show that the tensile stress of concrete can be effectively reduced by appropriately increasing the corbel height and ring beam width of the foundation. The results also show that the improved wind turbine foundation force is reasonable and can meet the use of the actual project requirements on the level of finite element analysis.

Keywords: onshore wind turbine foundation; damage evolution; concrete damage plasticity model (CDP); finite element method

Citation: Zhang, Z.; Liu, Q.; Chu, H.; Lacidogna, G.; Xu, J.; Cheng, H.; Liu, Z.; Jiang, W. Performance Analysis of an Improved Gravity Anchor Bolt Expanded Foundation. *Appl. Sci.* **2023**, *13*, 11181. https://doi.org/10.3390/app132011181

Academic Editor: Marek Krawczuk

Received: 10 August 2023
Revised: 7 October 2023
Accepted: 9 October 2023
Published: 11 October 2023

1. Introduction

With the continuous development of wind resources, the number of wind farms is increasing. Onshore wind power is a mature technology, and its development costs are much lower than that of offshore wind power. Figure 1 shows the installed capacity of global onshore and offshore wind farms from 2018 to 2022, according to statistics released by the Global Wind Energy Council (GWEC). Although the proportion of onshore wind farms has declined in the past two years, onshore wind farms still account for a large proportion of the entire wind power market [1]. Figure 2 shows the net new capacity of onshore wind power by country and region (2022–2024) [2]. Onshore wind power has continued to develop in the past five years, maximizing the power generation per megawatt installed capacity. In this process, as the fan becomes larger, the hub height becomes higher, the rotor diameter becomes larger, and the probability of the tower bending, the foundation overturning, the untimely replacement of anchor bolts, the deterioration of foundation cracks, and many other problems that will cause great harm to the fan increases. The market has put forward higher requirements for the safety performance of wind turbines. Therefore, the stress analysis and design of an onshore wind turbine's foundation structure are very important [3,4].

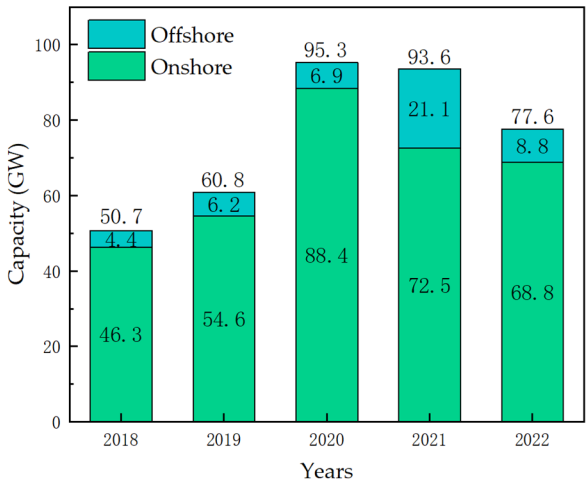

Figure 1. Installed capacities of onshore and offshore wind power plants worldwide from 2018 to 2022 (unit: GW).

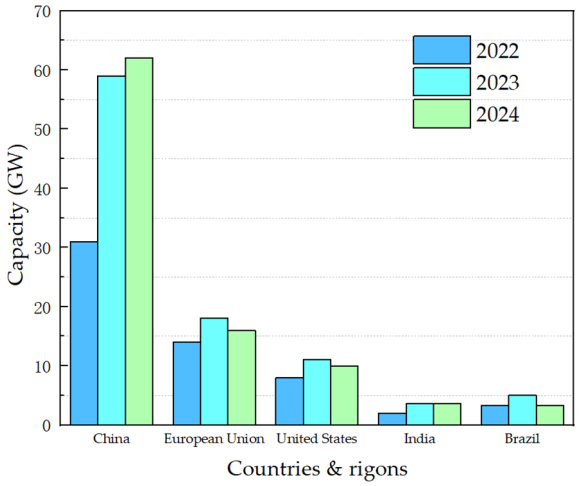

Figure 2. Net onshore wind electricity capacity additions by country or region, 2022–2024.

The working environment of wind turbines is very wet and harsh, which is because they are usually built in mountainous and open areas. The foundation is subjected to a combination of torque–vertical load–horizontal load–bending moment load (T-V-H-M) under operating conditions. The crack monitoring, fatigue damage, and vibration response of the wind turbine foundation have become the focus of research. Jack McAlorum et al. [5] proposed a method to determine and characterize the crack deterioration in the foundation of onshore wind turbines. Evans Amponsah, Zhiquan Wu et al. [6] used the double K crack propagation criterion to evaluate the stability of horizontal crack propagation in the foundation of an onshore wind turbine. Xue Bai, Minjuan He et al. [7] studied the fatigue behavior of an onshore wind turbine foundation and the influence of cyclic load on stress distribution. Bryan Puruncajas et al. [8] carried out structural health monitoring of an offshore wind turbine jacket foundation with only vibration response through a convolutional neural network. In addition, the study of structural vibration theory plays an important role in many fields of structure and foundation engineering [9–15]. The soil–structure interaction will cause a vibration response in the wind turbine foundation, which may cause damage to the foundation [16–18]. With the advent of the big data era, artificial intelligence [19–23] is gradually becoming an important tool in structural engineering and other fields. Jonathan De Anda et al. [24] proposed an optimization method for wind turbine towers and provided important design parameters for them.

The common tower types of wind turbines are steel towers, concrete towers, steel lattice towers, hybrid towers, and guyed rods [25]. Most onshore wind turbines are built on extended foundations, which are divided into gravity foundations and anchor pile foundations. As shown in Figure 3, there are two ways to connect the tower and the foundation in the extended foundation: one is to embed the tower directly into the concrete foundation slab ('foundation ring'); the other is to fix the bottom flange of the tower on the concrete by using prestressed bolts ('anchor cage ring') [26].

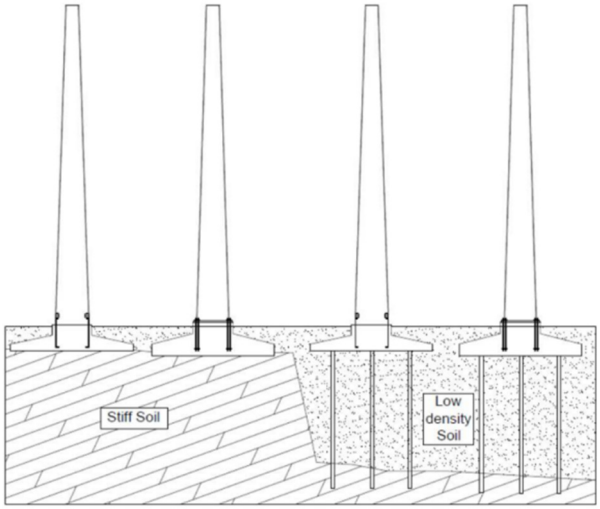

Figure 3. Wind turbine tower foundation configurations [27].

The foundation ring is widely used because of its simple structure, large production, convenient quality control, and convenient installation [28,29]. However, with the popularization and application of high hub and large capacity wind turbines, the anchor cage ring has gradually become the configuration used for the connection of large capacity wind turbines, with it replacing the foundation ring. As shown in Figure 4, the circular foundation [30–32] and annular foundation are both extended foundations, which are often used in wind turbines. However, both types of foundations are inconvenient for the maintenance and replacement of anchors.

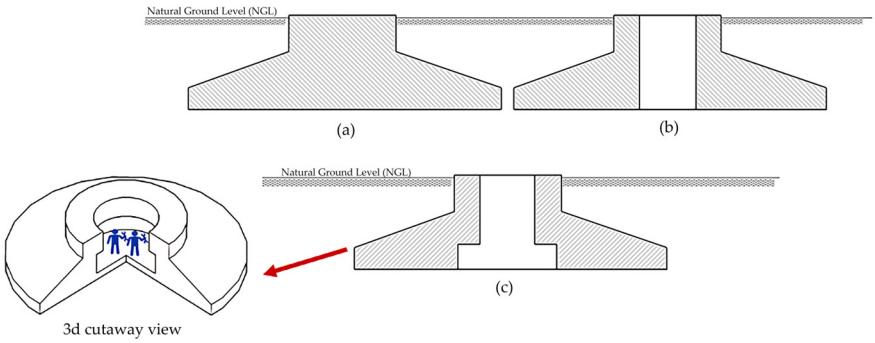

Figure 4. Schematic diagram of (**a**) a circular foundation, (**b**) a ring foundation under a towering structure, and (**c**) a ring wind turbine foundation under a concrete tower.

Therefore, this paper proposes an improved foundation form suitable for steel towers that expands the space in the lower area of the foundation, which is not only conducive to the maintenance and replacement of bolts but also reduces the cost of materials.

To facilitate the study, we selected a foundation in practical engineering and took its specific size, materials, and load parameters. Figure 5 shows the size parameters of the foundation and the details of the anchor bolts. A total of 192 anchor bolts were used on the foundation, which were evenly distributed in the overhanging part of the foundation.

Table 1 explains the meaning of the size parameters and the corresponding values. The size of the lower maintenance space can be changed by changing the parameters h1 and b3.

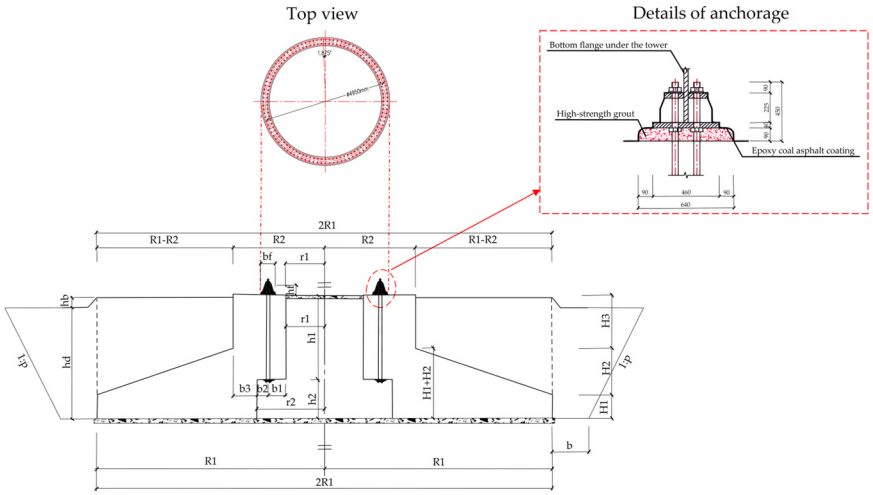

Figure 5. New turbine foundation size and anchor bolt details.

Table 1. The size of each part of the foundation.

Name	Sign	Value	Unit
Radius of the foundation plate	R_1	10.00	m
Radius of the foundation column	R_2	4.0	m
Foundation edge height	H_1	0.85	m
Variable cross-section height of the foundation	H_2	1.65	m
Column height	H_3	1.90	m
Upper cavity radius	r_1	1.7	m
Radius of the lower cavity	r_2	2.975	m
Upper cavity height	h_1	3.0	m
Lower cavity height	h_2	1.4	m
Distance between the ground bolt and the inner cavity	b_1	0.775	m
Distance from the ground bolt to the side wall	b_2	0.5	m
The thickness of the side wall of the column	b_3	1.025	m
Tower bucket force width	b_f	0.64	m
Load acting force elevation	H_f	0.465	m
Original buried depth of the foundation	h_d	3.9	m
Foundation backfill thickness	h_b	0.4	m
Excavation slope	P	1:0.5	/
Width of the foundation working face	b	1	m

The purpose of this paper is to study the influence of parameters h1 and b3 on the stress of the foundation via numerical simulation. According to the simple mechanical principle, the author puts forward a preliminary conjecture: when the load is constant, the maximum tensile stress value of the most dangerous place in the upper part of the foundation increases with the increase in h1 and decreases with the increase in b3.

2. Load Transfer Mechanism and Failure Mode

The load transfer mode of spread footing mainly relies on the bond between the foundation ring and the concrete, and the friction between the concrete and the side wall of the foundation ring to transfer the upper load to the lower foundation concrete. The foundation force characteristics, as well as the transfer characteristics, have been studied by scholars [33,34]. The damage around the steel ring of the spread footing is more obvious, which is prone to the problems of sliding of the steel ring and cracking of the surrounding concrete. The anchor foundation solves the above problems well. There is no contact

between the anchor rods and the concrete. There is usually a layer of pipe on the outside of the anchor. Both ends of the anchor are fixed to the surface of the upper and lower anchor plates. There is face-to-face hard contact between the anchor plate and the foundation. The bottom flange transfers the upper load to the foundation through the anchor. As shown in Figure 6, the moment can be converted into the pressure of the anchor ends on the concrete. The relationship between them is as follows:

$$M = P \cdot D_1 \quad (1)$$

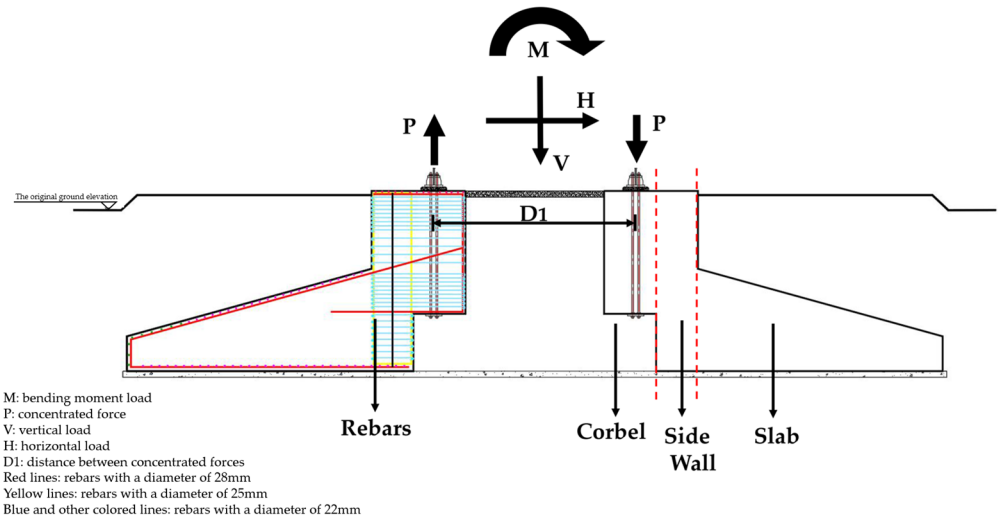

Figure 6. Load transfer schematic.

The vertical force is converted into a homogeneous pressure on the foundation of the flange. The torque and the horizontal force are mainly converted into shear forces on the anchor rod. The shear force is converted through the anchor into pressure on the concrete by the anchor. The foundation is always under pressure throughout the entire stressing process. This takes full advantage of the excellent compressive capacity of the concrete, thus avoiding tensile cracking of the concrete foundation around the foundation ring. In the event of corrosion or fracture of the anchor rods, the lower space can be accessed for timely replacement.

As shown in Figure 6, the annular foundation is divided into three parts: the corbel, side wall, and bottom plate. According to the specification, the reinforcement calculation of each part is completed. The upper load is transmitted to the side wall through the corbel of the foundation. Finally, it is transmitted to the foundation plate, causing the pressure to change between the foundation and the ground. The foundation may undergo structural damage under external loads. For example, the concrete cracking area being too large, the bolt being broken in a large area, punching failure, shear failure, local compression failure of the concrete, and so on. In addition, the separation area between the foundation and the soil, the Inclination of the foundation itself, the settlement of the foundation, and the inclination of the foundation should be strictly controlled.

As shown in Figure 4, (a) is the traditional ring foundation size and (b) is the new ring foundation. These foundations are considered gravity foundations that use the weight of the foundation and the weight of the backfill to resist overturning loads. The idea of using convex cavities is to reduce material costs and increase construction space. Compared with the traditional ring foundation, the new type of foundation has different stress and damage modes.

The wind turbine foundation test needs to consider the influence of loading boundary conditions, the scale model, and other factors. The test method has high time and economic costs, and the operation is complicated. Some scholars have studied the mechanical

characteristics and damage of wind turbine foundations by using numerical simulation. The accuracy of numerical simulation results is improved by considering the influence of the concrete plastic damage model, soil nonlinearity, mesh accuracy, and contact between different components [35–38]. Therefore, this paper mainly establishes a three-dimensional coupling model of anchor–foundation–soil through ABAQUS 2020. We mainly analyze the foundation detachment, foundation tilt, concrete and steel stress state, and tensile damage under extreme load conditions. The focus is to study the stress and structural damage of the new foundation, and to verify the feasibility of the reinforcement scheme. Furthermore, the influence of foundation size parameters h1 and b3 on the foundation's performance is studied by numerical simulation.

3. Finite Element Model

3.1. Modeling Materials

The model takes into account the foundation concrete, steel bars, high-strength grouting layer (HSGL), prestressed anchor cage, and soil. To improve the computational efficiency and reduce the tolerable accuracy, the details of the bolt hole and the anchoring end are not considered in the model. Table 2 shows the density ρ, elastic modulus E, Poisson ′s ratio ν, linear expansion coefficient α, and element type of various materials. The anchor rod in the foundation uses the cooling method to apply prestress. The other anchor plates and steel bars do not need to apply the corresponding prestress. The selection of parameters refers to the relevant specifications [39]. Only the soil and the concrete of the foundation part consider the nonlinearity of the material. We adopt the concrete damage plasticity (CDP) model for the concrete and the Mohr–Coulomb model for the soil. Table 3 shows the parameters of the Mohr–Coulomb model of soil. It is used because it is generally accepted and the parameters are easy to obtain [40,41]. All grids are structured. The unit types are mainly C3D8R (i.e., eight-node brick, reduced integration) and T3D2 (i.e., two-node 3D truss).

Table 2. Material parameters.

Material	ρ (kg/m^3)	E (MPa)	ν	α	Unit Type	Material Model
Concrete	2450	32,500	0.2	/	C3D8R	CDP
HSGL	2450	38,000	0.2	/	C3D8R	elasticity
Reinforcement	7850	200,000	0.3	/	T3D2	elasticity
Anchor plate	7850	206,000	0.3	/	C3D8R	elasticity
Anchor bar	7850	206,000	0.3	1.2×10^{-5}	T3D2	elasticity
Flange	7850	206,000	0.3	/	C3D8R	elasticity

Table 3. Parameters of the Mohr–Coulomb model in ABAQUS 2020.

Material	ρ (kg/m^3)	E (MPa)	ν	Angle of Dilation ψ (°)	Angle of Friction φ (°)	Cohesive Yielding Stress (kPa)	Absolute Plastic Strain
Soil	1800	50	0.3	0.1	30	50	0

3.2. Concrete CDP Model

The CDP model is a continuous, plastic-based damage model. It is often used for the damage analysis and crack distribution prediction of reinforced concrete structures. The model was proposed by Lubliner et al. [42] and then improved by Lee and Fenves [43]. The CDP model in ABAQUS can simulate the damage evolution of concrete conveniently and accurately. It is suitable for nonlinear compressive and tensile behavior. Therefore, we adopt this model for the foundation concrete in this study. It is assumed that the CDP model can determine the tensile and compressive behavior of concrete. Figure 7 shows the specific behavior of the model. The CDP model can be used to study the tensile cracking and

compression failure of wind turbine foundation concrete. Equations (2) through (10) give the stress—strain relationship of concrete under uniaxial tensile load and compressive load:

$$\sigma_t = (1-d_t)E_c\varepsilon \tag{2}$$

$$d_t = \begin{cases} 1-\rho_t\left[1.2-0.2x^5\right], & x \le 1 \\ 1-\frac{\rho_t}{\alpha_t(x-1)^{1.7}+x} & ,x > 1 \end{cases} \tag{3}$$

$$\rho_t = \frac{f_{t,r}}{E_c\varepsilon_{t,r}} \tag{4}$$

$$x = \frac{\varepsilon}{\varepsilon_{t,r}} \tag{5}$$

$$\sigma_c = (1-d_c)E_c\varepsilon \tag{6}$$

$$d_c = \begin{cases} 1-\frac{\rho_c n}{n-1+x^n}, & x \le 1 \\ 1-\frac{\rho_c}{\alpha_c(x-1)^2+x}, & x > 1 \end{cases} \tag{7}$$

$$\rho_c = \frac{f_{c,r}}{E_c\varepsilon_{c,r}} \tag{8}$$

$$n = \frac{E_c\varepsilon_{c,r}}{E_c\varepsilon_{c,r}-f_{c,r}} \tag{9}$$

$$x = \frac{\varepsilon}{\varepsilon_{c,r}} \tag{10}$$

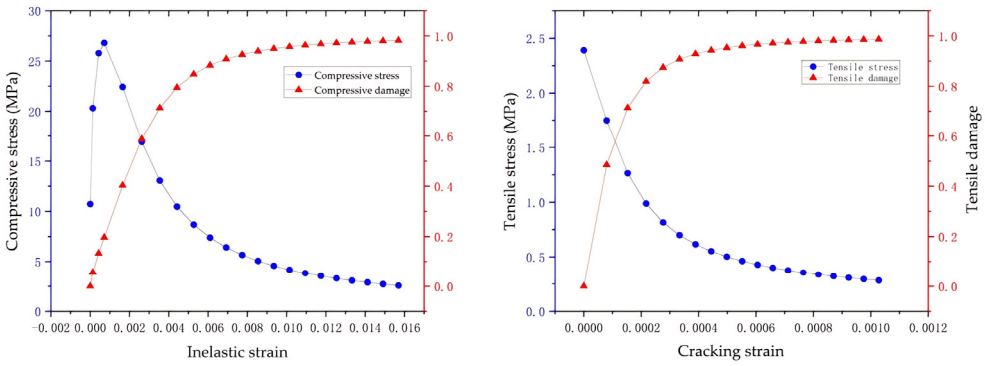

Figure 7. (**a**) Compressive behavior and (**b**) tensile behavior.

$\alpha_{t/c}$—parameter of the descending section of concrete uniaxial tensile/compressive stress–strain curve, given in the Code for Design of Concrete Structures in the United States, China, and other countries [39];

$f_{t/c,r}$—concrete uniaxial tensile/compressive strength;

$\varepsilon_{t/c,r}$—peak tensile/compressive strain of concrete corresponding to;

$d_{t/c}$—evolution parameter of concrete uniaxial tensile/compressive damage.

According to the energy equivalence hypothesis [44], the stress–strain relationship of materials can be expressed in terms of Equations (11) and (12). By substituting Equation (11) into Equation (2), Equation (13) can be obtained. By substituting (12) into (6), Equation (14) can be obtained. Figure 8 shows the stress–strain relationship and damage–strain relationship of the C40 concrete under uniaxial compression and tension. The specific damage

evolution parameters D_t and D_c with the CDP model are input into ABAQUS for further calculation. The calculation is easier to converge when D_t and D_c are used [45]. Table 4 shows some of the properties defined in ABAQUS for establishing the CDP model. The tensile damage parameters and compressive damage parameters obtained from the simulation results represent the severity of tensile damage and compressive damage of concrete elements. Before loading, the concrete has no tensile damage, and the parameter is 0. In the extreme stage close to the ultimate strength of the structure, the parameters are very close to 1. This represents complete damage to the foundation concrete.

$$\sigma_t = E_c (1 - D_t)^2 \varepsilon \quad (11)$$

$$\sigma_c = E_c (1 - D_c)^2 \varepsilon \quad (12)$$

$$D_t = 1 - \sqrt{1 - d_t} \quad (13)$$

$$D_c = 1 - \sqrt{1 - d_c} \quad (14)$$

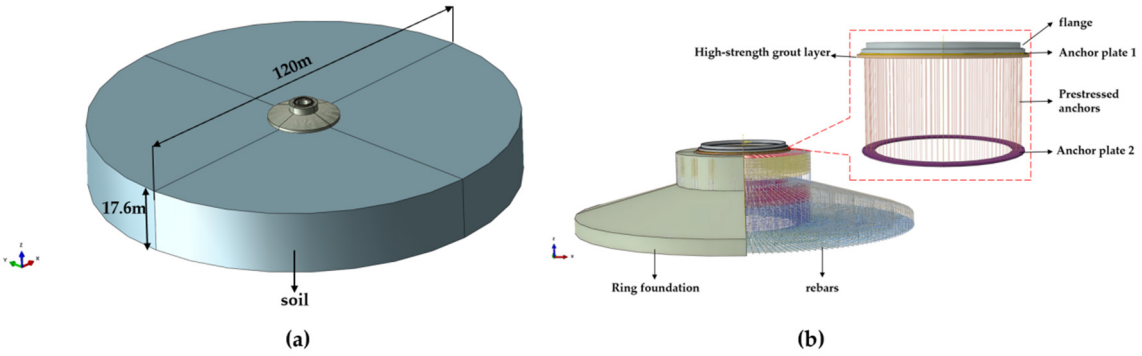

Figure 8. Finite element model: (**a**) foundation and soil and (**b**) details of the foundation.

Table 4. CDP model parameters.

Dilation Angle	Eccentricity	f_{b0}/f_{c0} (Biaxial/Uniaxial Ratio)	K	Viscosity Parameter
30°	0.1	1.16	0.667	0.004

The dilation angle and eccentricity are the parameters related to the yield surface flow rule. K is the influence parameter of concrete yield form; f_{b0} and f_{c0} are the biaxial compressive strength and uniaxial compressive strength of concrete, respectively, and the ratio of the two is the recommended value of the specification [39]; μ is the viscosity parameter defined in the CDP model. The larger it is, the easier the calculation is to converge, and the smaller it is, the higher the calculation accuracy is. When 0.0005 is taken, it can meet the requirements of accuracy and convergence at the same time.

3.3. Finite Element Model in ABAQUS

3.3.1. Finite Element Contact and Boundary Conditions

Figure 8 shows the details of the finite element 3D model. All the steel bars in ABAQUS are built into the foundation. The bottom surface of the high-strength grouting layer is bound to the top surface of the foundation. The bottom of the soil is completely fixed. The horizontal displacement of the soil side surface and the rotation of the *z*-axis are limited. The upper surface of the soil is completely free. To avoid the influence of the soil boundary effect [46], the soil model needs a large geometric size. In this paper, a geometric model of soil with a diameter of 120 m and a height of 17.6 m is established.

The model is a multi-interface contact finite element model. The setting of contact parameters determines the accuracy and convergence speed of the calculation. The surface contact settings in the model take into account the normal behavior and tangential behavior. In the tangential behavior, the friction formula uses a penalty method. The interface element method can better simulate complex geometric shapes and material properties, but it requires more computing time and memory space. The face-to-face contact method is more simple and easier to use. The reason why hard contact is used as normal behavior and friction is used as tangential behavior is that we pay more attention to the detachment and slip behavior between surfaces, which is of great significance to the safety of the foundation. Different friction coefficients are used between different materials, and the friction coefficient between the concrete and steel plate is set to 0.70 [47]. The friction coefficient between the steel plates is set to 0.80 [48]. The friction coefficient between the concrete and soil is assumed to be 0.40 [49]. Table 5 shows the contact parameters in ABAQUS.

Table 5. Contact parameters.

Contact Pair	Type	Tangential Behavior (Coefficient of Friction)	Normal Behavior
Flange–Anchor plate 1	Surface-to-surface contact	0.80	Hard contact
Anchor plate 1–HSGL		0.70	
Foundation–Anchor plate 2		0.70	
Foundation–Soil		0.40	

3.3.2. Loading Method and Analysis Steps

The model is subjected to a variety of forces including gravity, prestress, overburden pressure, vertical force V, horizontal force H, torque T, and bending moment M. The load used in the simulation is the extreme condition data in the existing project. The model is simplified, and the upper soil of the foundation is not modeled. The calculated uniform earth pressure is applied to the top of the foundation. The bending moment and concentrated force are applied to the center point of the top of the flange. The center point is coupled with the top surface of the flange. Figure 9 shows the details of the load application. Table 6 shows the specific value of the above load. The negative sign indicates the negative direction of the coordinate axis.

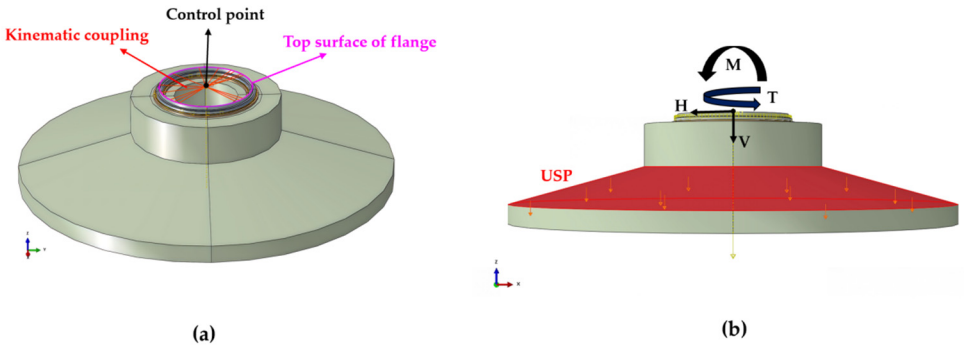

Figure 9. (**a**) Point-surface coupling and (**b**) location of the load.

Table 6. Load data under extreme conditions.

Gravity (m/s^2)	Uniform Distributed Soil Pressure (USP) (Pa)	V (kN)	H (kN)	T (kN·m)	M (kN·m)
−9.8	−49,371.4	−4779.86	−917.19	−7254.68	100,560.8

To obtain the initial stress of the prestressed anchor bolt, the model is simplified. The prestressed anchor bolt adopts the T3D2 element, which does not consider the modeling details of bolt holes and bolts so as to improve the calculation efficiency and reduce the tolerable accuracy. As shown in Figure 10, the unit is divided into three sections, and the upper and lower sections are built into the flange and anchor plate. Because there is no bond between the anchor bolt and the surrounding concrete, there is no constraint between the element of the middle section and the surroundings. The model uses the cooling method [50] to apply tensile stress to the prestressed anchor bolts, without considering the influence of the tensioning sequence, and applies tensile stress to all anchor bolts at the same time. The tension control stress Δ σ is calculated according to the following expression:

$$\Delta\sigma = E\alpha\Delta T \tag{15}$$

where E is the elastic modulus of the prestressed anchor bolt; α is the linear expansion coefficient of prestressed anchor bolt; and ΔT is the difference in the cooling temperature.

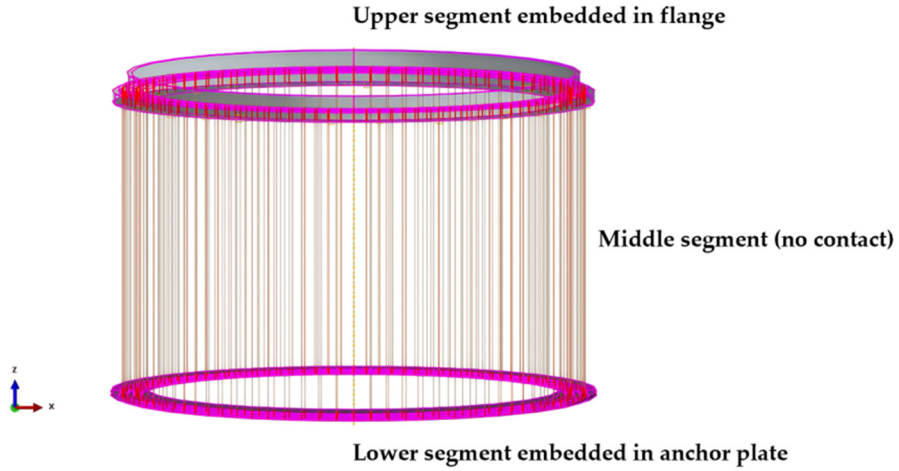

Figure 10. Constraints of the anchors.

The process of nonlinear analysis of the model includes six steps:

Step 0: Set up the in situ stress balance analysis step, only retain the soil components, calculate the displacement of the soil, and ensure that the displacement of the soil under the action of self-weight is small enough. The maximum vertical displacement of the model is 4.709×10^{-12}

Step 1: Activate the foundation and other components and apply gravity and earth pressure.

Step 2: The prestressed anchor bolt tension simulation.

Step 3: Apply vertical force *V*.

Step 4: Apply horizontal force *H*.

Step 5: Apply horizontal torque *T*.

Step 6: Apply bending moment *M* and the calculation is terminated when the specified load is applied.

4. Response of the Foundation

4.1. Stability of the Foundation

The wind turbine is different from general buildings, which belongs to the category of high-rise structures. It is mainly subjected to horizontal load. Slight surface inclination or uneven settlement of the foundation will cause a large horizontal deviation of the wind turbine, resulting in a large eccentric bending moment. When it is serious, it will bring greater security risks to the operation of the wind turbine. For this reason, we used ABAQUS to analyze the inclination and settlement of the improved foundation.

The bending moment from the upper support structure causes a large load eccentricity, which causes the bottom of the foundation to disengage from the soil. Figure 11 illustrates the finite element calculation results for the flange and foundation. The results show that the displacement field of the flange and foundation varies continuously and the contact pressure between the bottom of the flange and the bottom of the foundation increases gradually in the direction of the bending moment. No disconnection region was found.

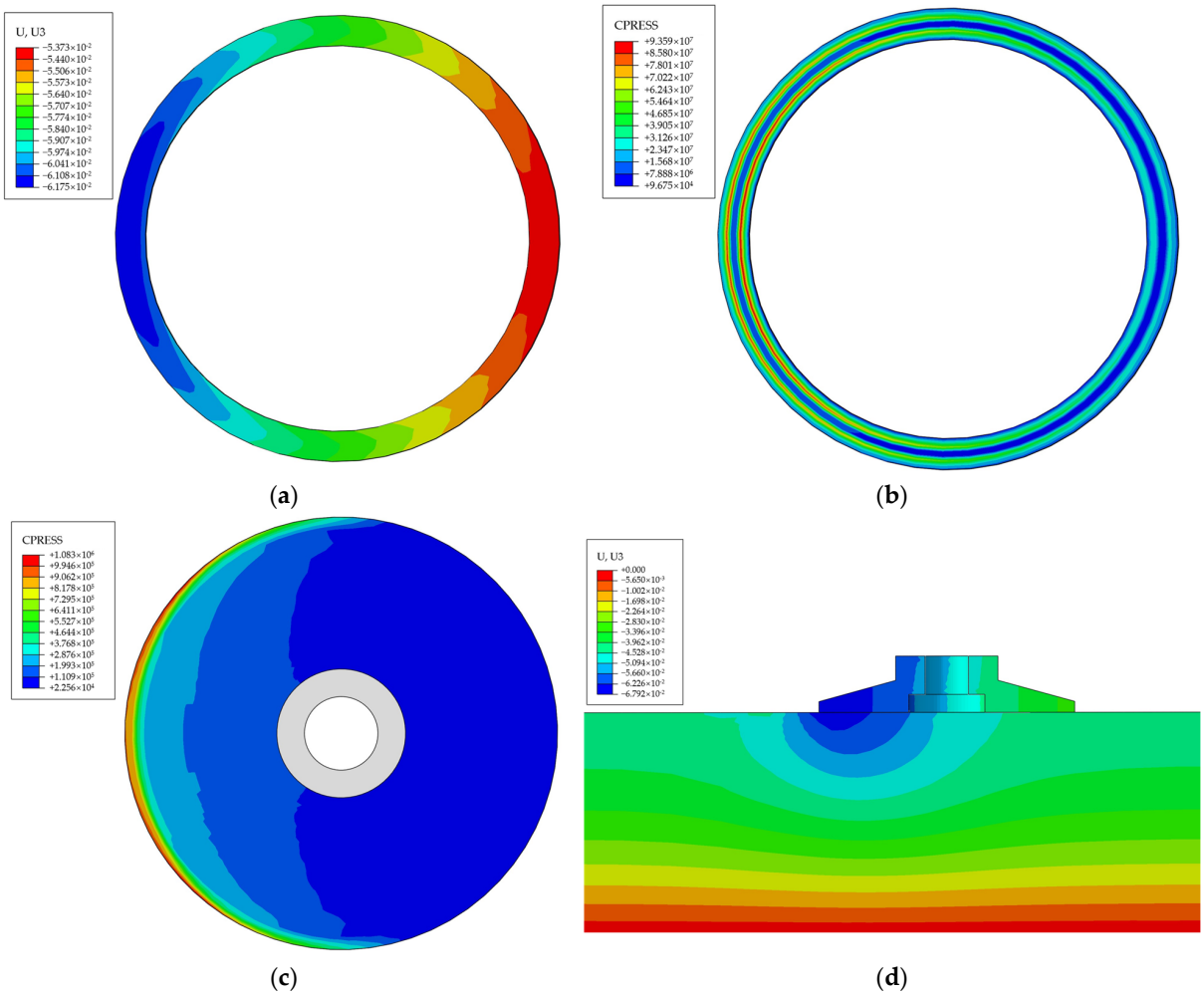

Figure 11. (**a**) Vertical displacement of the flange; (**b**) contact pressure on the bottom of the flange; (**c**) contact pressure on the bottom of the foundation; and (**d**) displacement clouds of the foundation and soil.

As shown in Figure 11d, three settlement observation points were selected for this simulation, including the left side, center point, and right side. The settlement–step curve of the foundation is shown in Figure 12a. The results show that the settlement of the center point of the foundation reaches 56.7 mm under analysis step 1 (self-weight effect), and the inclination of both the subsoil and the flange occurs in analysis step 6 (bending moment effect). The inclination is defined as the ratio of the maximum vertical displacement difference to the diameter distance. Figure 12b demonstrates the variation in the inclination of the subsoil and the flange. The results show that the inclination of the flange is always greater than the tilt of the lower soil and grows faster. The maximum inclination of the flange is 0.00166, and the maximum inclination of the lower soil is 0.00061, which is the inclination allowed by the Design Code for Wind Turbine Foundations for Onshore Wind Power Projects (NB/T 10311-2019).

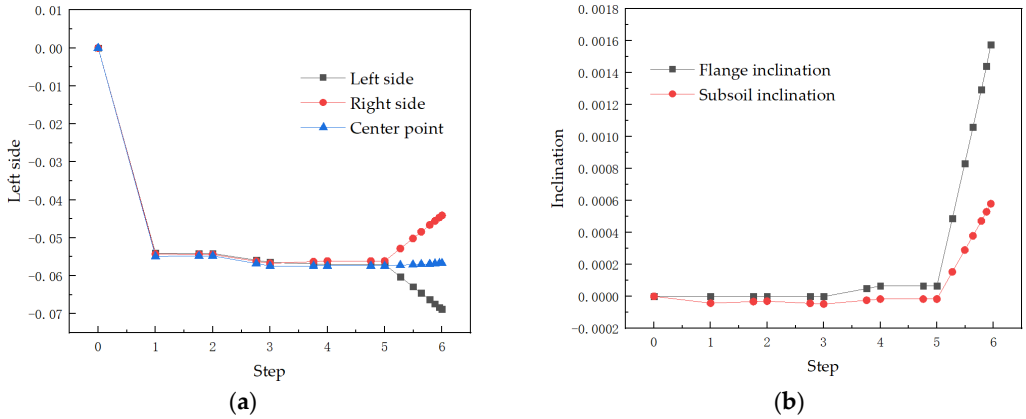

Figure 12. (**a**) Settlement change curves at the bottom of the foundation and (**b**) inclination curves of the flange and subsoil.

4.2. Foundation Stress Analysis

4.2.1. Stress Analysis of the Rebar

There are many kinds of steel bars in the foundation which mainly bear the tensile stress, and the collaborative concrete bears part of the pressure. Through the finite element calculation and analysis, the main force transmission characteristics of the foundation can be obtained. Through calculation and analysis, the stress distribution of the steel bar can be obtained in Figure 13. It can be seen that most of the steel bars are far from reaching the yield stress under extreme load conditions. Only the inner side of the radial reinforcement at the bottom plate cantilever has a large stress. The maximum value reaches 51.22 MPa. This part of the steel bar is mainly subjected to bending moment. The vertical reinforcement not only bears the compressive stress together with the concrete but also bears the tangential shear force and the bending moment generated by the horizontal load.

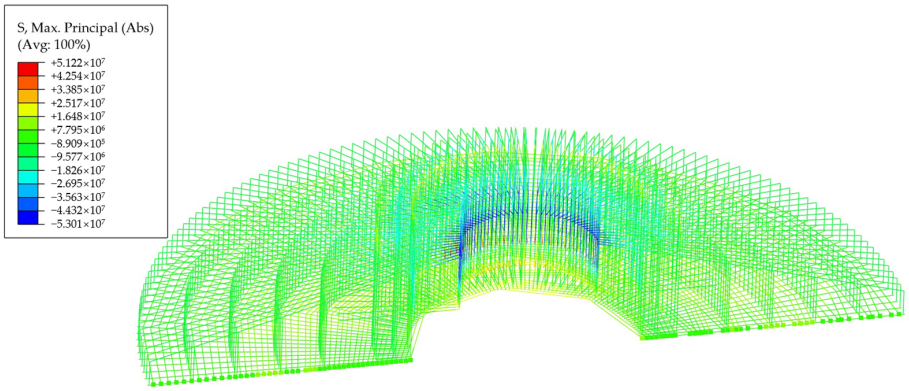

Figure 13. Stress distribution cloud of radial reinforcement.

Figure 14 shows the relationship between the stress of the radial steel bar at the cantilever of the bottom plate and the loading grade. It can be seen that the steel bar stress increases with the increase in the loading level. It is mainly divided into three stages. In the first stage, when the external load is small, the stress of the steel bar increases slowly. With the increase in the external load in the second stage, especially when the increase in bending moment is close to the extreme load, the stress growth rate is significantly enlarged. In the third stage, because the bending moment is no longer increased, the growth rate of steel bar stress is slowed down again. The stress gradually increases to the maximum value of 51.22 MPa. This shows that the steel bar here is mainly subjected to bending moment and is related to the stress state of the concrete. The steel bars are far from reaching the yield stress. There is still a lot of room for optimization of the engineering quantity of steel

bars. Therefore, we can reduce the use of steel bars on the foundation slab and the outside of the column according to the needs of the actual project.

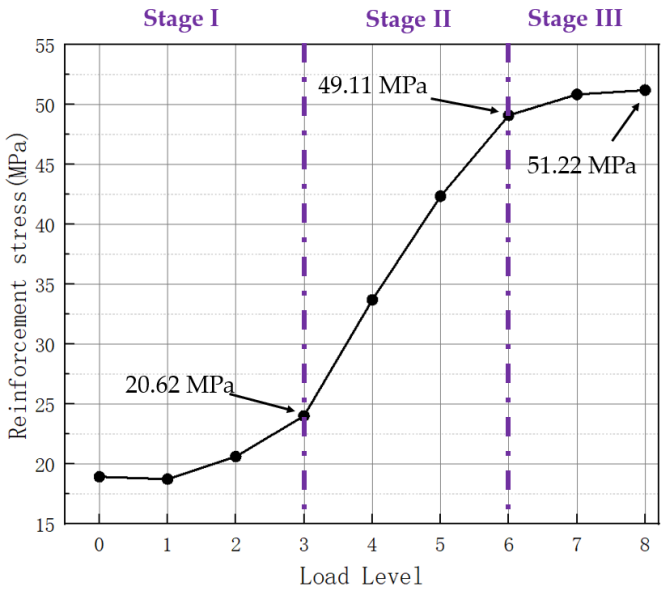

Figure 14. Relationship between reinforcement stress and load level.

4.2.2. Damage Analysis of Concrete

It is necessary to understand the development process of foundation damage in order to analyze the safety performance of structures. This can highlight the relatively weak parts of the structure. To study the failure response of the new wind turbine foundation under load, this paper studies the distribution of the tensile damage factor (DAMAGET) of the foundation under different loads based on the plastic damage constitutive model of concrete. The evolution and development process of damage at different positions of the foundation with the increase in load was revealed.

During the loading process, the damage development distribution of the new foundation is as shown in Figure 15. It can be seen from Figure 15 that, during the loading process of the new wind turbine foundation, the damage first appears in the upper part of the inner side of the foundation ring wall. With the increase in the load to 50%, the damage also occurred at the neck of the foundation and the corbel. When the load is further increased to 75%, the damage is further extended to the lower part of the foundation ring wall and the bottom surface of the foundation. When the load is fully applied, the damage area of the above parts is further expanded, and the maximum value of the tensile damage factor appears at the foundation corbel, with a maximum value of 0.98.

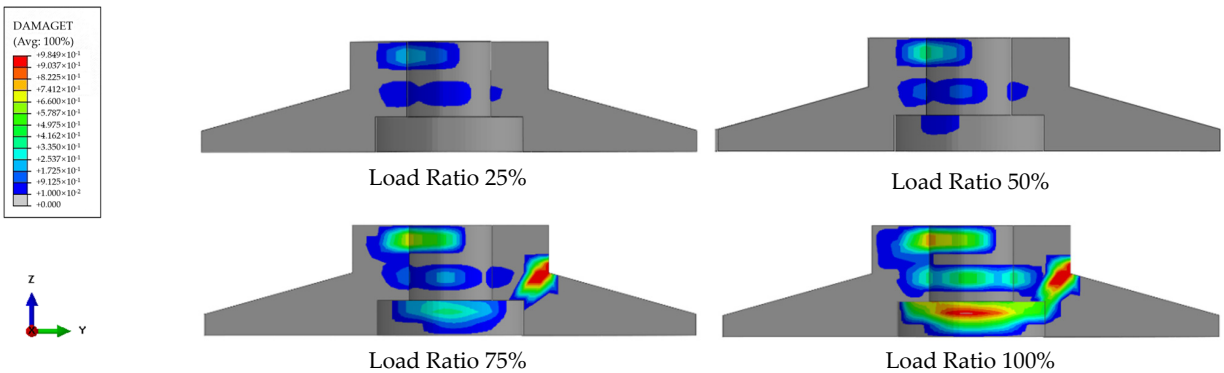

Figure 15. Foundation damage distribution.

To obtain a more detailed change rule of new foundation damage, this paper selects several feature points of different parts of the foundation, and we gradually increase the load ratio (from 0 to 100%). The change in the tensile damage factor at the feature points was observed. The feature points and damage changes are shown in Figure 16.

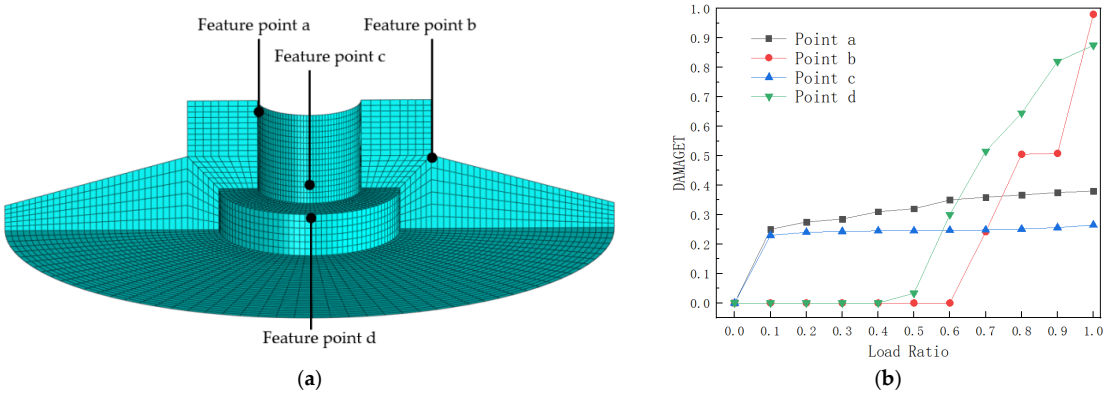

Figure 16. (**a**) Foundation feature points and (**b**) damage evolution.

From Figure 16, it can be seen that when the wind load is transmitted to the new foundation, the upper part of the foundation ring wall (point a) and the lower part of the foundation ring wall (point c) are first damaged. After the wind load exceeds 10%, the damage at points a and c increases slowly. When the wind load is applied to 60%, the damage begins to occur at the neck of the foundation (point b). The tensile damage factor increases sharply to the maximum at this time. When the wind load is applied to 70%, the cantilever root (point d) of the foundation slab is destroyed. The tensile damage factor increases rapidly here.

The above analysis shows that the damage of the foundation is mainly concentrated in the plate of the foundation and the foundation ring wall. The tensile failure coefficient of the inner side of the bottom plate reaches the maximum value of 0.98 when the load is fully applied. When the external load gradually increases from 10% to 100%, the damage inside the foundation slab starts from scratch and eventually spreads throughout the whole foundation. Therefore, it is very necessary to increase the stress reinforcement here when reinforcing the reinforcement.

4.3. Size Change Analysis

The calculation results of the ABAQUS finite element model show that the damage to the foundation is mainly concentrated in the column of the foundation. The corbel height h1 and the ring beam width b3 were changed. Thus, five schemes of the foundation were obtained. The maximum tensile stress of each part of the foundation of five different schemes under ultimate load was further analyzed to obtain a better scheme. The corbel height h1, the ring beam width b3, and each part of the selected foundation are shown in Figure 17.

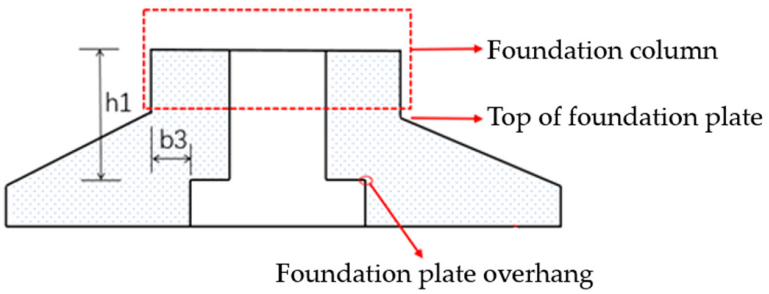

Figure 17. Schematic illustration of the corbel height and ring beam width.

The corbel height h1 of scheme 1, scheme 2, and scheme 3 is kept as 3000 mm. The width of the ring beam b3 increases by 250 mm in turn. The maximum tensile stress of the foundation column, the top of the bottom plate, the bottom of the bottom plate, and the cantilever of the bottom plate under the ultimate load is calculated using ABAQUS. The results are shown in Table 7.

Table 7. Stress response of various parts of the foundation with different ring beam widths.

	h1 /mm	b3 /mm	Maximum Tensile Stress of the Foundation Column/MPa	Maximum Tensile Stress at the Bottom of the Foundation Slab/MPa	Maximum Tensile Stress at the Top of the Foundation Slab/MPa	Maximum Tensile Stress of the Foundation Slab Overhang/MPa
Option 1	3000	1025	2.223	2.23	2.37	2.23
Option 2	3000	1275	2.21	2.333	2.231	2
Option 3	3000	1525	1.99	2.395	1.89	1.537

As shown in Figure 18, when the width of the ring beam b3 increases from 1025 mm to 1525 mm, the maximum tensile stress of the foundation column, the top of the bottom plate, and the cantilever of the bottom plate decrease to varying degrees. From the finite element analysis results and the evolution process of the foundation stress, increasing the width of the ring beam can increase the bending volume of the concrete, and the shape of the foundation tends to be uniform, which reduces the stress concentration of the concrete at the above position due to the sudden change in size. We think that this is the reason why increasing the width of the ring beam can reduce the tensile stress of the concrete at many places in the foundation.

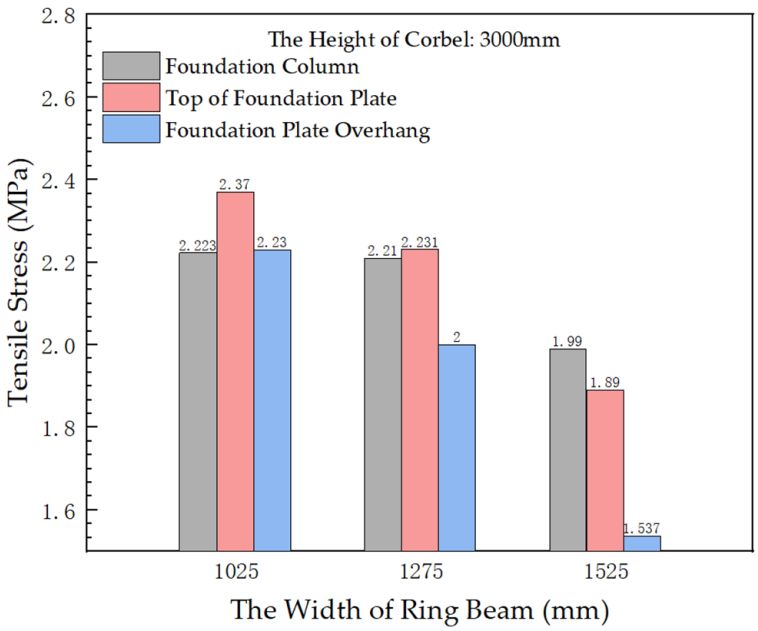

Figure 18. Stress response of foundations with different ring beam widths.

The ring beam width b3 of scheme 1, scheme 4, and scheme 5 is maintained at 1025 mm. The width of the ring beam h1 is reduced by 250 mm in turn. The maximum tensile stress of the foundation column, the top of the bottom plate, the bottom of the bottom plate and the cantilever of the bottom plate under the ultimate load was calculated using ABAQUS. The results are shown in Table 8.

Table 8. Stress response of various parts of the foundation with different corbel heights.

	h1 /mm	b3 /mm	Maximum Tensile Stress of the Foundation Column/MPa	Maximum Tensile Stress at the Bottom of the Foundation Slab/MPa	Maximum Tensile Stress at the Top of the Foundation Slab/MPa	Maximum Tensile Stress of the Foundation Slab Overhang/MPa
Option 1	3000	1025	2.223	2.23	2.37	2.23
Option 4	2750	1025	2.185	2.272	2.265	2.2
Option 5	2500	1025	2.174	2.335	2.201	2.181

As shown in Figure 19, when the corbel height h1 increases from 2500 mm to 3000 mm, the maximum tensile stress of the foundation column, the top of the bottom plate, and the cantilever of the bottom plate increases to varying degrees. This is probably because as the corbel height increases, the concrete bending moment at these positions also increases, resulting in an increase in the maximum tensile stress. The tensile stress at the top of the bottom plate increases most obviously.

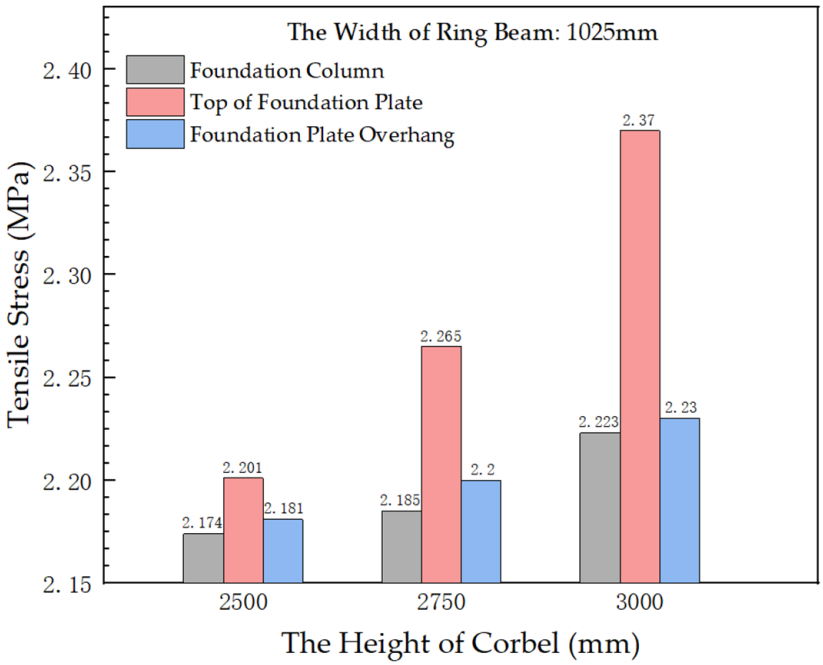

Figure 19. Stress response of foundations with different corbel heights.

5. Conclusions

In this study, an improved prestressed anchor ring foundation scheme is proposed. The nonlinear analysis of the refined model of the foundation under the upper extreme operating condition load is systematically carried out. The results of foundation stability analysis and the damage development law of foundation materials are obtained. The influence of the foundation size parameters is further studied. In general, the maximum tensile stress on the upper part of the foundation shows a significant increase or decrease trend with the size of the foundation, and the foundation form is reasonable.

Specific conclusions are as follows:

(1) The improved foundation has good stability. The foundation can maintain a small disengagement and tilt under extreme operating loads.

(2) The steel bar stress of the improved foundation under extreme operating load conditions is lower than the yield stress. The feasibility of the reinforcement scheme is verified. At the same time, it is pointed out that the stress of the steel bar increases greatly at the junction of the column and the bottom plate.

(3) The upper bending moment load is the main reason for the damage of foundation materials. The material damage of the foundation is mainly concentrated in the foundation plate and the junction of the foundation plate and the column. The material damage process is a ductile damage process.

(4) With the change in foundation size, the stress changes for the concrete in the different upper parts of the foundation are obvious. Under the condition that other dimensions of the foundation remain unchanged, increasing the width of the ring beam (b3) can effectively reduce the maximum tensile stress of the foundation column, the top of the bottom plate, and the cantilever of the bottom plate. The maximum tensile stress at these places also increases with an increase in corbel height (h1).

Due to the limitation of working space, the research on the improved wind turbine foundation presented in this paper remained at the level of finite element analysis. It is hoped that, in the future, the safety of the improved wind turbine foundation can be supported by experiments.

Author Contributions: Conceptualization, Z.Z., H.C. (Hongmin Chu), J.X. and Q.L.; methodology, Q.L. and Z.Z.; formal analysis, Q.L., Z.L., H.C. (Haiyang Cheng) and W.J.; investigation, G.L., Z.L., H.C. (Haiyang Cheng) and W.J.; writing—original draft preparation, Z.L., H.C. (Haiyang Cheng) and W.J.; writing—review and editing, G.L.; supervision, J.X.; project administration, Z.Z.; funding acquisition, J.X. All authors have read and agreed to the published version of the manuscript.

Funding: This research was funded by Shandong Electric Power Engineering Consulting Institute Corp (grant number: 2023GKF-0270) and 111 Projects (B20039). And The APC was funded by Tianjin University.

Institutional Review Board Statement: Not applicable.

Informed Consent Statement: Not applicable.

Data Availability Statement: Due to the nature of this research, participants of this study did not agree for their data to be shared publicly, so supporting data is not available.

Conflicts of Interest: The authors declare no conflict of interest.

References

1. *Global Wind Report 2023*; Global Wind Energy Council: Brussels, Belgium, 2023.
2. *Renewable Energy Market Update Outlook for 2023 and 2024*; International Energy Agency: Paris, France, 2023.
3. Guo, Y.; Zhang, P.; Ding, H.; Le, C. Design and verification of the loading system and boundary conditions for wind turbine foundation model experiment. *Renew. Energy* **2021**, *172*, 16–33. [CrossRef]
4. Negro, V.; López-Gutiérrez, J.-S.; Esteban, M.D.; Matutano, C. Uncertainties in the design of support structures and foundations for offshore wind turbines. *Renew. Energy* **2014**, *63*, 125–132. [CrossRef]
5. McAlorum, J.; Perry, M.; Fusiek, G.; Niewczas, P.; McKeeman, I.; Rubert, T. Deterioration of cracks in onshore wind turbine foundations. *Eng. Struct.* **2018**, *167*, 121–131. [CrossRef]
6. Amponsah, E.; Wu, Z.; Feng, Q.; Wang, Z.; Kwame Mantey, S. Analysis of crack propagation in onshore wind turbine foundations using the double-K fracture model. *Structures* **2022**, *41*, 925–942. [CrossRef]
7. Bai, X.; He, M.; Ma, R.; Huang, D.; Chen, J. Modelling fatigue degradation of the compressive zone of concrete in onshore wind turbine foundations. *Constr. Build. Mater.* **2017**, *132*, 425–437. [CrossRef]
8. Puruncajas, B.; Vidal, Y.; Tutivén, C. Vibration-Response-Only Structural Health Monitoring for Offshore Wind Turbine Jacket Foundations via Convolutional Neural Networks. *Sensors* **2020**, *20*, 3429. [CrossRef]
9. He, B.; Feng, Y. Vibration Theoretical Analysis of Elastically Connected Multiple Beam System under the Moving Oscillator. *Adv. Civ. Eng.* **2019**, *2019*, 4950841. [CrossRef]
10. Kiani, K. Nonlocal discrete and continuous modeling of free vibration of stocky ensembles of vertically aligned single-walled carbon nanotubes. *Curr. Appl. Phys.* **2014**, *14*, 1116–1139. [CrossRef]
11. Kiani, K. Nonlocal and shear effects on column buckling of single-layered membranes from stocky single-walled carbon nanotubes. *Compos. Part B Eng.* **2015**, *79*, 535–552. [CrossRef]
12. Kiani, K. Free vibration of in-plane-aligned membranes of single-walled carbon nanotubes in the presence of in-plane-unidirectional magnetic fields. *J. Vib. Control* **2016**, *22*, 3736–3766. [CrossRef]
13. Li, Y.X.; Gong, J. Free and forced vibration analysis of general multiple beam systems. *Int. J. Mech. Sci.* **2022**, *235*, 107716. [CrossRef]

14. Mao, Q. Free vibration analysis of elastically connected multiple-beams by using the Adomian modified decomposition method. *J. Sound Vib.* **2012**, *331*, 2532–2542. [CrossRef]
15. Stojanović, V.; Kozić, P.; Janevski, G. Exact closed-form solutions for the natural frequencies and stability of elastically connected multiple beam system using Timoshenko and high-order shear deformation theory. *J. Sound Vib.* **2013**, *332*, 563–576. [CrossRef]
16. Wang, L.; Zhong, R.; Liu, L. Resonance characteristics of onshore wind turbine tower structure considering the impedance of piled foundations. *Arab. J. Geosci.* **2020**, *13*, 163. [CrossRef]
17. Deng, Z.-W.; Fan, Z.-J.; Zhou, Y.-M.; Deng, P.-Y. Study on Dynamic Response Characteristics of Circular Extended Foundation of Large Wind Turbine Generator. *Sustainability* **2022**, *14*, 14213. [CrossRef]
18. Harte, M.; Basu, B.; Nielsen, S.R.K. Dynamic analysis of wind turbines including soil-structure interaction. *Eng. Struct.* **2012**, *45*, 509–518. [CrossRef]
19. Du, H.; Du, S.; Li, W. Probabilistic time series forecasting with deep non-linear state space models. *CAAI Trans. Intell. Technol.* **2023**, *8*, 3–13. [CrossRef]
20. Fan, B.; Zhang, Y.; Chen, Y.; Meng, L. Intelligent vehicle lateral control based on radial basis function neural network sliding mode controller. *CAAI Trans. Intell. Technol.* **2022**, *7*, 455–468. [CrossRef]
21. Shahin, M. State-of-the-art review of some artificial intelligence applications in pile foundations. *Geosci. Front.* **2014**, *7*, 33–44. [CrossRef]
22. Valença, J.; Mukhandi, H.; Araújo, A.G.; Couceiro, M.S.; Júlio, E. Benchmarking for Strain Evaluation in CFRP Laminates Using Computer Vision: Machine Learning versus Deep Learning. *Materials* **2022**, *15*, 6310. [CrossRef]
23. Zhang, W.; Li, H.; Li, Y.; Liu, H.; Chen, Y.; Ding, X. Application of deep learning algorithms in geotechnical engineering: A short critical review. *Artif. Intell. Rev.* **2021**, *54*, 5633–5673. [CrossRef]
24. De Anda, J.; Ruiz, S.E.; Bojórquez, E.; Inzunza-Aragon, I. Towards optimal reliability-based design of wind turbines towers using artificial intelligence. *Eng. Struct.* **2023**, *294*, 116778. [CrossRef]
25. Zafar, U. *Literature Review of Wind Turbines*; Bauhaus Universität: Weimar, Gemany, 2018; 41p.
26. Stavridou, N.; Efthymiou, E.; Baniotopoulos, C.C. Verification of Anchoring in Foundations of Wind Turbine Towers. *Am. J. Eng. Appl. Sci.* **2015**, *8*, 717–729. [CrossRef]
27. de Groot, J. Multiaxial Compressive Stress States within a Concrete Onshore Wind Turbine Foundation: A three Dimensional Non-Linear Finite Element Analysis of the Concrete Surrounding the Anchor Cage. Master's Thesis, Delft University of Technology, Delft, The Netherlands, 2022.
28. Currie, M.; Saafi, M.; Tachtatzis, C.; Quail, F. Structural health monitoring for wind turbine foundations. *Proc. Inst. Civ. Eng. Energy* **2013**, *166*, 162–169. [CrossRef]
29. Currie, M.; Saafi, M.; Tachtatzis, C.; Quail, F. Structural integrity monitoring of onshore wind turbine concrete foundations. *Renew. Energy* **2015**, *83*, 1131–1138. [CrossRef]
30. Frederick, D. On Some Problems in Bending of Thick Circular Plates on an Elastic Foundation. *J. Appl. Mech.* **2021**, *23*, 195–200. [CrossRef]
31. Mindlin, R.D. Influence of Rotatory Inertia and Shear on Flexural Motions of Isotropic, Elastic Plates. *J. Appl. Mech.* **2021**, *18*, 31–38. [CrossRef]
32. Reissner, E.; Reissner, J.E. A problem of unsymmetrical bending of shear-deformable circular ring plates. *Ing. Arch.* **1985**, *55*, 57–65. [CrossRef]
33. Amponsah, E.; Wang, Z.; Kwame Mantey, S. Bending-bearing behaviour of embedded steel ring-foundation connection of onshore wind turbines. *Structures* **2021**, *34*, 180–197. [CrossRef]
34. Lian, J.; Ding, H.; Zhang, P.; Yu, R. Design of large-scale prestressing bucket foundation for offshore wind turbines. *Trans. Tianjin Univ.* **2012**, *18*, 79–84. [CrossRef]
35. Deshpande, V.M. Numerical Modelling of Wind Turbine Foundations Subjected to Combined Loading. Master's Thesis, The University of Western Ontario (Canada), Ontario, CA, Canada, 2016.
36. Gaihre, N. Analytical and Numerical Modeling of Foundations for Tall Wind Turbine in Various Soils. Master's Thesis, Southern Illinois University at Carbondale, Carbondale, IL, USA, 2020.
37. Madandoust, R.; Kazemi, M. Numerical analysis of break-off test method on concrete. *Constr. Build. Mater.* **2017**, *151*, 487–493. [CrossRef]
38. Martinelli, P.; Flessati, L.; Dal Lago, B.; Fraraccio, G.; di Prisco, C.; di Prisco, M. Role of numerical modelling choices on the structural response of onshore wind turbine shallow foundations. *Structures* **2022**, *37*, 442–458. [CrossRef]
39. Ministry of Housing and Urban Rural Delevelopment of The People's Republic of China. Code for Design of Concrete Structures. In *Basic Provisions for Structural Components*; China Architecture & Building Press: Beijing, China, 2010; Volume GB50010-2010.
40. Imanzadeh, S.; Pantet, A.; Taibi, S.; Ouahbi, T. Soil Behavior Under Onshore Wind Turbine Foundation-Case Study in Brazil Using New French EOLIFT Technology. *Adv. Civ. Eng. Technol.* **2021**, *4*, 594. [CrossRef]
41. Ma, H.; Chen, L. Static And Dynamic Analysis Modeling For Offshore Wind Turbine Foundation Structures. In Proceedings of the Ninth ISOPE Pacific/Asia Offshore Mechanics Symposium, Busan, Republic of Korea, 14–17 November 2010.
42. Lubliner, J.; Oliver, J.; Oller, S.; Oñate, E. A plastic-damage model for concrete. *Int. J. Solids Struct.* **1989**, *25*, 299–326. [CrossRef]
43. Lee, J.; Fenves, G.L. A plastic-damage concrete model for earthquake analysis of dams. *Earthq. Eng. Struct. Dyn.* **1998**, *27*, 937–956. [CrossRef]

44. Krajcinovic, D.; Fonseka, G.U. The Continuous Damage Theory of Brittle Materials, Part 1: General Theory. *J. Appl. Mech.* **1981**, *48*, 809–815. [CrossRef]
45. Xiao, Y.; Chen, Z.; Zhou, J.; Leng, Y.; Xia, R. Concrete plastic-damage factor for finite element analysis: Concept, simulation, and experiment. *Adv. Mech. Eng.* **2017**, *9*, 1687814017719642. [CrossRef]
46. Ullah, S.N.; Hu, Y.; Stanier, S.; White, D. Lateral boundary effects in centrifuge foundation tests. *Int. J. Phys. Model. Geotech.* **2017**, *17*, 144–160. [CrossRef]
47. Rabbat, B.G.; Russell, H.G. Friction Coefficient of Steel on Concrete or Grout. *J. Struct. Eng.* **1985**, *111*, 505–515. [CrossRef]
48. Alsharhan, A.S. *Handbook of Physical Quantities*; Routledge: London, UK, 1997.
49. Khazaei, J.; Amiri, A.; Khalilpour, M. Seismic evaluation of soil-foundation-structure interaction: Direct and Cone model. *Earthq. Struct.* **2017**, *12*, 251–262. [CrossRef]
50. Yan, J.; Lin, Y.; Wang, Z.; Fang, T.; Ma, J. Failure mechanism of a prestressed concrete containment vessel in nuclear power plant subjected to accident internal pressure. *Ann. Nucl. Energy* **2019**, *133*, 610–622. [CrossRef]